Published in: *Journal of Flow Visualization and Image Processing,* Vol. 29, No. 2. pp. 1-26, 2022

Fluid Flow Observations of the Spray Near-Field using High-Speed X-ray Imaging

Julie K. Bothell[1], Timothy B. Morgan[1], Alan L. Kastengren[2], and Theodore J. Heindel[1*]

[1]Center for Multiphase Flow Research and Education and Department of Mechanical Engineering, Iowa State University, USA

[2]X-ray Science Division, Advanced Photon Source, Argonne National Laboratory, USA

Abstract

Sprays are important to may industrial processes, but the near-field region where spray formation takes place is difficult to visualize and characterize through visible light imaging because this region is typically optically dense. X-ray imaging is one technique that can penetrate this optically dense region and provide unique observations of the spray formation process. This study uses high-speed white beam X-ray imaging conducted at the Advanced Photon Source to capture spray formation dynamics from a canonical airblast atomizer. A range of momentum flux ratios are visualized by varying the gas flow rate while the liquid flow rate is held constant. The use of X-rays show overlapping flow structures including bags, ligaments, mushrooms, and webs. Air bubbles are captured within the liquid regions, and a very dynamic crown forms at the liquid needle exit at higher momentum flux ratios. Finally, at the highest

* Corresponding Author: Theodore J. Heindel
Department of Mechanical Engineering
Iowa State University
2043 Black Engineering
2529 Union Drive
Ames, IA 50011-2161
theindel@iastate.edu

momentum flux ratios, air bubbles and liquid droplets are observed migrating upstream in the center of the crown, and this motion is attributed to a toroidal recirculation cell at the nozzle exit.

Keywords: Atomization, high-speed imaging, primary breakup, spray, synchrotron, X-ray diagnostics

1 Introduction

Sprays are found in many natural and industrial settings, from rain and breaking ocean waves to liquid fuel combustion and additive manufacturing. In typical applications, when liquid is ejected from a nozzle in a gaseous environment and sufficient shear is available, the liquid is broken up into to a liquid-gas spray. The resulting spray is commonly divided into three regions. The near-field region is closest to the nozzle exit and is generally composed of a dense liquid core or sheet that undergoes breakup into ligaments, which then undergo additional breakup into individual liquid droplets. The spray mid-field region is usually composed of a dispersion of liquid ligaments undergoing breakup and individual liquid droplets that may undergo secondary breakup. Finally, the far-field region contains a dilute dispersion of individual liquid droplets that continue to disperse radially and axially as they travel from the nozzle exit. While the far-field region has been well characterized, primary breakup and the near-field region has been minimally investigated because the thick liquid core and large structures render the region nearly impenetrable to visible light. However, the near-field region is vital to understanding sprays because it controls and sets the primary combustion zone for fuel sprays (Lightfoot et al., 2015). Additionally, it provides the initial conditions as the spray enters the secondary breakup region.

The spray mid- and far-field regions can be quantified using optical- and laser-based methods like shadowgraphy, back-illuminated or backlit imaging, Phase Doppler Particle Analysis (PDPA), or Particle Image Velocimetry (PIV) (Bachalo, 2000; Castrejón-Pita et al.,

2013; Fansler and Parrish, 2015; Settles and Hargather, 2017). The challenge of using these techniques in the near-field is that the spray is usually optically dense in this region; hence, other techniques are required like X-ray imaging (Heindel, 2018; Kastengren and Powell, 2014; Kastengren et al., 2012; Linne, 2012a, 2012b, 2013). Unlike visible light, X-rays are able to penetrate the dense liquid near-field region. The X-ray attenuation (absorption) in this dense region is related to the amount and density of material through which the beam passes. The attenuation can be used to quantity the amount of material present in the line of sight along the X-ray beam using Beer-Lambert's Law (Li et al., 2019). One additional advantage of X-rays is the slight refraction and diffraction at liquid-gas interfaces, which can actually enhance visualization in a technique called phase contrast imaging (Heindel, 2018; Kastengren et al., 2012).

Traditional radiography is the act of obtaining a shadow-like image of an object using penetrating radiation such as X rays or γ-rays, where darker regions correspond to where the object is more dense and/or thicker (Cartz, 1995); a simple medical X-ray showing bone structure is a radiograph. X-ray computed tomography is when radiographs of an object are acquired from several hundred viewing directions and then reconstructed with standard algorithms to show intensity variations of the object cross-section (Hampel, 2015; Hsieh, 2003).

X-rays have been used to visualize multiphase flows for many years (Aliseda and Heindel, 2021; Heindel, 2011). They are typically generated using one of two methods: (i) an electron beam hitting a metal target like that found in traditional tube sources, or (ii) a synchrotron light source. The high-speed X-ray imaging in this paper was produced using the synchrotron facility at the Advanced Photon Source (APS) at Argonne National Laboratory. X-rays produced by a synchrotron source are polychromatic, like those produced by tube

sources, but they are highly collimated and produce a much higher X-ray flux (up to 6 orders of magnitude higher (Matusik et al., 2019)). X-rays produced with a synchrotron source are found only at selected facilities like APS (Kastengren and Powell, 2014; Kastengren et al., 2012; Tekawade et al., 2020).

There are several X-ray imaging techniques that can be used to characterize sprays (Heindel, 2018). White beam radiography or white beam imaging can be completed using a synchrotron source. White beam imaging uses the high intensity X-ray beam from the synchrotron that is composed of a range of energies (wavelengths), similar to white light being composed of a range of wavelengths in the visible spectrum. Once the beam passes through the object of interest, it is detected by a scintillator crystal that luminesces visible light proportional to the amount of absorbed X-ray energy. The luminescence is imaged using a turning mirror into a high-speed digital camera that is shielded from the X-rays. White beam imaging has been used to investigate, for example, the liquid core dynamics of a high momentum ratio spray (Machicoane et al., 2019), the two phase flow behavior in an opaque beryllium injector (Lin et al., 2017), the mixing of an impinging jet spray (Halls et al., 2017), and the gas-liquid interface of a turbulent liquid jet being injected into still air (Osta et al., 2012).

A subset of white beam imaging is called X-ray Phase Contrast Imaging (XPCI), which requires a high-energy coherent X-ray beam like the white beam at a synchrotron facility. XPCI is based on the differences between the refractive index of a sample and its environment. The X-ray beam passes through the object of interest (i.e., fluid flow) and is allowed to propagate some distance past it. A phase shift is produced at the interface of two materials with a high density difference, like a gas-liquid interface, creating a Fresnel diffraction pattern that enhances the absorption contrast at the interface; the enhanced absorption contrast can be used to facilitate

image analysis to quantify flow features. XPCI has recently been used to explore the flow through a fuel injector (Moon et al., 2015), the cavitation dynamics in a high-speed nozzle (Karathanassis et al., 2021), and venturi flows (Khlifa et al., 2017; Zhang et al., 2020a; Zhang et al., 2020b).

Tomographic imaging of multiphase flows has been summarized in recent reviews (Aliseda and Heindel, 2021; Heindel, 2011). This imaging modality has also been applied to sprays. To acquire the necessary number of image projections, either the source and detector have to revolve around the spray (Halls et al., 2014; Li et al., 2017b), the spray has to rotate within the imaging region (Coletti et al., 2014; Tekawade et al., 2020), or multiple source-detector pairs have to be arranged around the spray (Halls et al., 2019; Rahman et al., 2018).

This paper describes the flow structures from a canonical airblast atomizer that are visualized using high-intensity X-rays, which allows for high-speed flow visualization (up to 100 kHz in this study). While the liquid flow rate is held constant, the gas flow rate is varied to provide a range of momentum flux ratios, where the shear imposed on the liquid increases with increasing momentum flux ratio, creating highly dynamic aperiodic flows, which are discussed below.

2 Experimental Setup

The experimental setup for this study consists of two major components, the flow loop (discussed in Section 2.1) and the X-ray imaging setup (discussed in Section 2.3). Additionally, the non-dimensionalized flow parameters are defined in Section 2.2 and a brief discussion on the X-ray image processing can be found in Section 2.4.

2.1 Nozzle and Flow Loop

The spray used in this study is generated using a canonical two-fluid airblast atomizer shown in Figure 1. The inner aluminum liquid needle has an ID of d_l = 2.1 mm and OD of D_l = 2.7 mm at the tip, and is coaxial with an outer air chamber (d_g = 10 mm ID at the tip). Two identical outer air chambers are used in this work, one fabricated from aluminum and the other fabricated from acetal plastic. The aluminum outer nozzle allows enough X-ray signal through to view the internal flow (see, for example, Machicoane et al. (Machicoane et al., 2019) for a static image or Li et al. (Li et al., 2017a) for a video). The acetal plastic nozzle has a precision copper ring at the exit and is used as an electrical grounding path for a separate study involving electrostatics; the copper ring prevents X-ray visualization inside the nozzle. Complete details of the nozzle design are found elsewhere (Huck et al., 2018; Machicoane and Aliseda, 2017; Machicoane et al., 2019).

Air and water are used as the two fluids in the airblast atomizer. The air and water flow loops have been detailed elsewhere (Bothell et al., 2020a; Li et al., 2019) and only a summary is provided here. Compressed air is provided through the building supply and is filtered prior to entering the flow loop. After the filter, the air is partitioned into two lines, each of which has a pressure regulator to limit the air pressure that is fed to the system. One of the compressed air lines is used to feed air to the nozzle, while the second is used to pressurize a water tank to provide the water to the nozzle. A ball valve on each of the air lines is used to close the air line when not in use.

The air feed line is partitioned a second time to direct the air flow as “co-flow” and “swirl” air (see Figure 1). Electronic proportioning valves and air flow meters are located after this partition and are used to control and monitor the air flow rates. Each co-flow and swirl air

line passes through air flow meters and then each are further split into four identical lines that are then attached to the upper portion of the nozzle to provide air flow into the test nozzle. The four co-flow lines impinge onto the liquid needle longitudinal axis, across the four quadrants, producing a purely coaxial gas stream at the nozzle exit. The four swirl lines enter the air nozzle in the same plane as the co-flow lines, but tangent to the air nozzle wall, introducing swirl in the gas stream. When swirl is added to the gas, the total gas flow rate remains constant, diverting part of the total gas from the co-flow to the swirl injection.

The second air line is fed into the water tank to create a pressurized section of air on top of the water that provides the force necessary to push the water through the water line. From there, the water passes through a water flow meter and an electronic proportioning valve and then enters the liquid needle. The liquid needle is designed to produce fully developed laminar Poiseuille flow and has $L/d_l \approx 50$.

The electronic proportioning valves and flow meters are connected to a data acquisition system that provides real time measurement and control. The electronic proportioning valves are each controlled by a proportional, integral, and derivative (PID) control system implemented in an in-house LabView program. Values from the flow meters are sent to the data acquisition system and used as feedback, as well as stored so that any observed phenomenon can be related back to the instantaneous flow measurement.

2.2 Flow Parameters

The total liquid (Q_l), co-flow (Q_{NS}), and swirl (Q_{SW}) flow rates are measured during each test, where the total air flow rate $Q_{total} = Q_{NS} + Q_{SW}$. The ratio of swirl air flow rate to co-flow air flow rate is defined as the swirl ratio (SR) to quantify the amount of air entering the gas nozzle through the tangential ports relative to the amount entering perpendicular to the liquid needle:

147 $$SR = \frac{Q_{SW}}{Q_{NS}} \quad (1)$$

148 In this work, most observations are provided with SR = 0; a few cases are shown with SR = 1.
149 Note that the total gas flow rate remains constant when the swirl ratio is varied.

150 The liquid Reynolds number is defined as:

151 $$Re_l = \frac{U_l d_l}{\nu_l} \quad (2)$$

152 where U_l is the mean exit velocity of the liquid and ν_l is the kinematic viscosity of water. The gas
153 Reynolds number is defined as:

154 $$Re_g = \frac{U_g d_{eff}}{\nu_g} = \frac{U_g \sqrt{d_g^2 - D_l^2}}{\nu_g} \quad (3)$$

155 where U_g is the mean exit velocity of the gas, defined as Q_{total}/A_g with A_g the total gas exit area;
156 ν_g is the kinematic viscosity of air; and d_{eff} is the gas effective diameter at the nozzle exit,
157 defined as the diameter of a circle with the exit area equal to A_g.

158 The momentum flux ratio is defined as:

159 $$M = \frac{\rho_g U_g^2}{\rho_l U_l^2} \quad (4)$$

160 where the subscripts g and l represent the gas and liquid properties, respectively, and ρ is the
161 fluid density.

162 Finally, a Weber number for the flow can also be defined based on the mean slip velocity
163 and the liquid nozzle exit diameter:

164 $$We = \frac{\rho_g \left(U_g - U_l\right)^2 d_l}{\sigma} \quad (5)$$

165 where σ is the surface tension of water.

All cases investigated in this work held the liquid flow rate constant at $Re_l = 1{,}100$ while the gas flow rate is varied such that $21{,}300 \leq Re_g \leq 180{,}000$, yielding $6 \leq M \leq 440$ and $39 \leq We \leq 2{,}900$. This corresponds to actual mean fluid velocities at the nozzle exit of $U_l = 0.48$ m/s and 34 m/s $\leq U_g \leq 290$ m/s.

2.3 X-ray Imaging

The high-speed flow visualization in this paper is completed over four separate experimental campaigns at APS; this facility uses synchrotron technology to provide high brilliance X-ray beams that can be used for flow visualization (Kastengren and Powell, 2014; Kastengren et al., 2012). APS works by accelerating electrons to nearly the speed of light and then bending the path of the electrons. When the electron path is bent by a bending magnet, wiggler, or undulator to change their direction, they emit an X-ray beam that is tangent to the direction of motion. The 7-BM beam line is used throughout this study, which provides high intensity white beam X-rays that can be used for 2D radiographic imaging with microsecond or sub-microsecond time resolution (Halls et al., 2017), and can produce very detailed 2D spatially and temporally resolved measurements of highly dynamic 3D events, like spray formation.

The setup for APS white beam radiography is shown in Figure 2. A broadband X-ray beam is first emitted from the synchrotron ring. It then, optionally, passes through a set of filters to reduce soft X-rays and beam hardening, or to reduce the beam flux, if desired. The beam then passes through a rotating chopper wheel to further reduce the time-average power of the beam. The chopper wheel is composed of two 15.2 cm diameter, 6.35 mm thick copper discs with two "pie wedge" openings cut into each disc. The discs are arranged such that a common open wedge of about 7.9° was used. The discs are spun at 0.5 Hz, yielding bursts of X-rays at 1 Hz. Although

188 the chopper wheel is used to limit the average beam intensity, the acetal plastic nozzle still
189 suffered radiation damage at the end of the last imaging campaign (Heindel et al., 2019).
190 After passing through the chopper wheel, the beam passes through the spray where the
191 intensity of the beam decreases, depending on the amount of fluid through which it passes. The
192 beam is then detected by a scintillator crystal. In this study, either a 500 μm thick YAG:Ce or a
193 100 μm thick LuAG scintillator crystal is used, depending on the test condition. Each scintillator
194 crystal luminesces in the visible spectrum with an intensity proportional to the X-ray intensity.
195 The visible light is then reflected by a mirror into a high-speed digital camera where an image is
196 taken. The mirror is necessary because X-rays that are transmitted through the scintillator crystal
197 could damage the camera if it is in the beam path. Additionally, shielding is placed around the
198 imaging equipment to shield it from scattered X-rays that could damage the camera electronics.
199 In this study, one of two high-speed cameras are used. The first is a Photron FASTCAM
200 Mini AX50 with a frame rate of 2 kHz at full field of view (1024 × 1024 pixels). The second is a
201 Photron FASTCAM SA-Z with a frame rate of 20 kHz at full field of view (1024 × 1024 pixels).
202 In most cases, the cameras are operated using a reduce field of view to increase the frame rate.
203 The cameras are connected to 105 mm – 50 mm or 180 mm – 50 mm macro-coupled lens
204 combinations, respectively, to provide an effective magnification of 2.1x or 3.6x. At the highest
205 SA-Z frame rates (100 kHz), a 1.4x teleconverter is also added to the lens combination to yield
206 an effective magnification of 5.04x. Frame rates typically varied from 6 kHz for the slowest flow
207 rates using the AX50 to 100 kHz for the highest flow rates using the SA-Z, with exposure times
208 ranging from 1.05 μs to 3.75 μs, respectively.
209 Note the white beam in the 7-BM beam line at APS is not square (~8 mm wide by ~6 mm
210 tall), and the intensity is most uniform in the beam center and then drops off toward the top and

bottom edges. Furthermore, the spray is much larger than the X-ray beam and most imaging is completed using a reduced field of view to utilize a higher camera frame rate and a more uniform beam flux. Hence, the beam center was the preferred imaging location. Additionally, to capture a wider spray region, a quasi-checkerboard imaging pattern is used to image several discrete locations. As illustrated in Figure 3, a backlit image of the airblast nozzle spray shows a large spray extent while the white boxes show a quasi-checkerboard pattern used for white beam imaging of the same spray. The exact image size and checkerboard pattern depends on the specific camera, its image settings, and the area of interest within the spray. This study focuses on the near-field region and most white beam imaging is within 10 liquid needle diameters (about 2 gas nozzle diameters or 20 mm) or less from the nozzle exit. Furthermore, as the momentum flux ratio increased, the number of axial locations decreased because a full spray formed closer to the nozzle exit. Finally, the (x, y) coordinates of any given image represent the image center, where x is in the spray axial direction in mm, y is in the spanwise direction in mm, and (0, 0) represents the nozzle exit on the centerline of the liquid needle.

2.4 Image Normalization and Resolvable Object Size

Normalization of X-ray images helps to eliminates static bias which improves the image quality. Normalization is generally the first step in pre-processing the images for further analysis. Flat field normalization is used for this study and is defined by (Van Nieuwenhove et al., 2015):

$$N = \frac{(P - D)}{(F - D)} \tag{6}$$

where P represents the original image, D is a dark field image, F is the flat field image, and N is the new normalized image. The mathematical operations in Eq. (6) are performed pixel-by-pixel. The dark field image is an image taken with no light entering the camera. The flat field image is created by taking a series of background images from a region where there is no spray or nozzle.

In practice, a sequence of background images (typically 400 frames) are acquired and averaged together to produce a flat field image with minimal noise. Additionally, as the cameras used in this study have a built-in calibration that does the dark field compensation onboard the camera, an ideal image of all zeros is used for the dark image.

From a visual inspection of the white beam images used in this study, the minimum resolvable object size is 5 pixels in diameter (20-25 μm, depending on camera and lens combination). Factors that affect the minimum resolvable object size include image resolution, contrast between the droplets and the background compared to the amount of noise that is present, and sources of error such as distortion and blurring which can be ignored in favor of the visual validation. The maximum resolvable object size is limited by the maximum size of droplet that can fit within the imaging frame.

3 Results and Observations

To show the advantages of X-ray imaging of sprays with respect to visible light imaging, Section 3.1 compares the visible features of a spray with M = 6 and SR = 1 between backlit imaging and X-ray white beam imaging. Section 3.2 makes overall comparisons of how the spray near-field changes as the momentum flux ratio is increased. Finally, the detailed features of spray breakup and changes in the liquid core are examined in Section 3.3.

3.1 Advantages of X-ray Imaging

Historically, backlit or shadowgraph imaging has been a popular method for studying the near-field region of a spray (Castrejón-García et al., 2011; Castrejón-Pita et al., 2013; Dash et al., 2018; Settles and Hargather, 2017). However, white beam X-ray radiography has recently gained traction because the technique provides information-rich images and enables rapid data collection. The high intensity of the X-ray beam makes it possible to have a short exposure so

that fast-moving sprays can be captured without blur. The constant beam flux during image acquisition also allows images to be taken with high-speed cameras, and therefore the movement of the spray can be visualized (Li et al., 2017a). X-rays attenuate as they pass through liquid, so the resulting image can be correlated to the amount of liquid along the beam path (Li et al., 2019). Hence, the X-ray image is a 2D projection of the liquid content along the beam path, where the gray scale variation correlates to liquid thickness, which provides information in the depth dimension. In contrast, backlit or shadowgraphy imaging uses visible light that reflects and refracts off of the gas-liquid interface and provides a binary image that shows where the projected liquid is, or is not, present, but provides no information on the amount of liquid in the image depth direction.

Figure 4 shows a comparison of a backlit image to white beam X-ray images for a spray with M = 6 and SR = 1. It is important to note that backlit imaging can easily cover a larger spray area than synchrotron-based white beam imaging, but tube source X-rays can be used to capture large spray regions if there is a sufficient signal-to-noise ratio in the images (Heindel, 2018; Li et al., 2019). The major difference between backlit and white beam imaging, which is important for analysis, is the level of detail that is available. Backlit imaging can provide a long imaging sequence and intact length and spray angle can be easily determined from the images (Bothell et al., 2020a; Bothell et al., 2020b; Morgan and Heindel, 2021). However, the resulting images only show the presence of liquid (a shadow), and liquid thickness cannot be determined. Additionally, if multiple fluid structures like overlapping droplets exist along the light path, they appear as a single object in the recorded backlit image. In contrast, for X-ray images like those shown in Figure 4, the thicker liquid corresponds to the darker region. The greyscale level can be correlated to the optical depth of the liquid region (Li et al., 2019), so the darker the region, the

more liquid is present between the X-ray source and detector. This also allows the ability to identify overlapping flow structures. The benefits of white beam X-ray images over backlit images are very apparent at the nozzle exit, as shown in Figure 4b. In this region, X-rays allow imaging inside the outer aluminum air nozzle. The liquid needle walls are also identified. There is also clear evidence of liquid wicking up the outside of the water needle (see the large arrow marked with "A" in Figure 4b), which is impossible to capture with backlit imaging. Further downstream, air bubbles within the liquid region and overlapping liquid structures are also visible (Figures 4c and 4d, respectively). The enhanced white regions at the air-water interface are also visible in the X-ray images and are due to phase contrast effects (Heindel, 2018).

3.2 Overall Spray Observations and Comparisons

Figure 5 shows various white beam images at selected spray locations for three different momentum flux ratios. Since the images are acquired in a checkerboard fashion (see Figure 3), they are uncorrelated. For each flow condition, the image size may also differ and is a function of the camera and frame rate, but the physical scale is consistent across all images to show the trade-offs between frame rate and image size. Note the images presented in Figure 5 (and all subsequent images) represent a typical image from the respective region, and all described observations represent a compilation of observations after viewing several hundred to several thousand images for each flow condition and location. Finally, the liquid flow rate is held constant at Re_l = 1,100 for each condition, SR = 0, and the gas flow rate is increased to increase the momentum flux ratio.

The top image for all momentum flux ratios shows the approximate location of the liquid needle exit as the dark vertical lines, and the edge of the copper grounding ring from the acetal plastic nozzle is visible at the very top of the image. Focusing initially on the M = 6 images, bag

303 formation is easily captured as the water and air exit the nozzle. The bags breakup into ligaments
304 as they progress downstream, which breakup into droplets. Increasing the gas flow rate such that
305 the momentum flux ratio increased by a factor of 5 (M = 30) and then by another factor of 5
306 (M = 150), shows that the extent of the intact liquid region downstream of the nozzle exit gets
307 shorter as the momentum flux ratio increases. Additionally, the flow structures that are observed
308 downstream get smaller and more dispersed. More details on these structures are provided
309 below.

310 **3.3 Qualitative Description of Spray Breakup**

311 The following is a detailed qualitative description of spray breakup for sprays with
312 various momentum flux ratios. Spray dynamic descriptors follow common identifiers, when
313 available. If a name does not exist for a particular dynamic, then identifiers are chosen to best
314 represent the given dynamic structure.

315 3.3.1 Airblast atomizer with M = 6

316 When M = 6 and SR = 0, a slowly oscillating liquid stream is observed right at the liquid
317 nozzle exit. Some of the water wicks up the outside of the liquid nozzle (Heindel, 2018); X-rays
318 allow for this observation because they penetrate the opaque nozzle. As the spray progresses
319 downstream, instabilities form along the gas-liquid interface where the gas tries to penetrate the
320 liquid, forming bags as shown in Figure 5 at M = 6. The bag grows and deforms the liquid jet
321 leading to ligament formation, shown in Figure 6a as structures identified as “A”. As the bag
322 thins, ligaments form that are connected by a thinning liquid sheet. As the liquid moves further
323 downstream, the liquid sheet continues to thin and eventually ruptures, shown in Figure 6a as
324 structures identified as “B”. Figure 6b has been enlarged to emphasize the edge of a liquid sheet
325 (“B”) right before rupture. When bag breakup occurs, ligaments and many small droplets (with

respect to the size of the ligaments) form. The thinnest portion of the bag produces the smallest droplets whereas the thicker edge of the bag generates the ligaments and larger droplets.

The liquid ligaments eventually separate from the main liquid stream at a distance known as the intact length (where the continuous liquid region is no longer observed). The intact length is not a constant value, but has sharp oscillations where a ligament may form at the tip and then abruptly break off. Because white beam imaging of the spray is completed in sections, and the intact length may span more than one image region, it is challenging to provide a precise measure with the imaging technique employed here. A comparison of intact length measures with different techniques has been completed for the sprays shown here (Bothell et al., 2020a).

As ligaments continue downstream, they can be stretched by the high-speed air surrounding them, increasing the ligament speed with downstream distance. This also leads to secondary bag and ligament formation, as shown in Figure 6c with the structures identified as "C"; these structures continually stretch, become thinner, and eventually breakup into smaller droplets.

The separated ligaments stretch as they move downstream, but the process is not uniform. For example, Figure 7 shows an image sequence of ligament stretching and breakup, where the time between frames is 555 μs (several frames are omitted between each image). Bulges in the ligament "A" are connected by thin liquid regions. The bulges grow and the connecting regions thin and eventually rupture, as shown by "B" and "C", where the bulges form droplets, identified by "D". The breakup process forms nonuniform droplets as well as many satellite droplets, as shown by the enhanced image region and objects identified as "E".

The motion of the ligaments is quite dynamic, with different parts of the ligament moving at different velocities. They can stretch axially, collapse axially to form mushroom shaped

structures (Fig. 8a), or tumble. Horizontal ligaments generally stretch more in the middle to create a U-shape and then break apart. These structures may rupture further along different paths, depending on if they are large or small. The larger mushroom structures often split into secondary ligaments, or the upper and lower portions separate into two droplets. Smaller mushroom structures often form a bag before breaking into smaller droplets.

A unique phenomenon that is visible using X-ray imaging, but not shadowgraphy or backlit imaging, is air bubbles trapped inside liquid regions. When bubbles form because of bags folding on the edge of the liquid stream, they move significantly slower than the rest of the liquid, and some have been observed to migrate upwards towards the nozzle exit. Larger bubbles may disappear as the liquid separates into ligaments and droplets. Smaller bubbles often get trapped inside the liquid and move with it. Examples of air bubbles inside the liquid are highlighted in Figure 8, where they are found in the observed mushroom structure, inside a liquid ligament, and inside individual droplets. Bubbles trapped inside liquid droplets could have a significant effect on the combustion process if the spray was a fuel injector. Bubbles could also create hollow metal powders from liquid metal sprays that could be detrimental to additive manufacturing processes (Anderson et al., 2018).

In addition to breakup, the liquid structures (ligaments, bags, mushrooms, liquid sheets, and droplets) sometimes collide with each other. During collisions, the masses often combine; they either remain as a single droplet or may undergo secondary breakup downstream. A series of images showing droplet collision is provided in Figure 9, where several image frames are omitted from this sequence to provide a representation of the collision process.

Similar spray structures continued to form and breakup throughout the near-field region until the spray is broken into many droplets. Once the spray is composed of only droplets, the

droplet size distribution begins to stabilize. Secondary atomization, with droplets breaking apart into smaller droplets, may still occur, but at a slower rate than primary atomization. Droplets that are most likely to break up during secondary atomization are typically larger and the breakup is caused by instabilities that form on the droplet surface. When secondary breakup occurs, the droplets first deform into a thin oblong shape. The center region of the oblong shape narrows as the ends are pulled apart. Once the center of the oblong shape becomes thin enough, the droplet will suddenly break apart into two droplets, usually of similar size. The droplets move with approximately the same downstream velocity but continue moving further away from each other after breakup. One or more satellite droplets may also form between the larger separated droplets, where the satellite droplets are much smaller than the two main droplets. A typical example of this process is shown in Figure 10, where the secondary breakup of two droplets are observed simultaneously. Note the time between each image is 1.1 ms.

3.3.2 Airblast atomizer with M = 30

Many of the phenomena that are observed from the airblast atomizer at M = 6 are also captured when M = 30, but the liquid breakup occurs much faster and closer to the nozzle exit, which results in smaller downstream droplets. With a more active spray region, some of the breakup mechanics are too fast to capture in sequence unless the frame rate is greater than 45 kHz. The higher momentum flux ratio also results in more interference with overlapping spray dynamics.

When the momentum flux ratio increases to M = 30 and SR = 0, wicking around the nozzle is not visible from white beam X-ray radiographs as it was with M = 6. Necking occurs in the attached liquid portion of the spray very near the liquid nozzle exit, identified as “A” in Figure 11a with the narrowest point 0.5-1.0d_l downstream of the exit plane. Ligament formation

and eventual separation is observed after the narrowing liquid region, identified as “B” in Figure 11a. The separation and breakup of ligaments is rapid in comparison to a spray with M = 6, and a larger number of liquid sheets and bags are present in the spray region just below the liquid necking.

In sequential images in regions like that of Figure 11a, the majority of the mass appears to oscillate back and forth across the 2D image projection. It is hypothesized that the oscillation is more of a 3D helical flow with the direction varying in a chaotic manner. Stereographic imaging is needed to confirm this. However, manual tracking of the liquid motion shows that the motion did not follow a sinusoidal pattern. In comparison to the spray with M = 6, a spray with M = 30 has ligaments that are much narrower, but still create liquid sheets between the ligaments before they quickly break apart. With the increased shear forces from the higher gas flow rate, the ligaments become very thin so that when they do break, much smaller droplets are observed compared to those at M = 6.

At the higher gas flow rate, liquid sheets form at a high rate where some rejoin with liquid ligaments and others become bags that break apart into small droplets. The droplets that form from the bag rim are larger than those that form from the bag, but they are still smaller than those observed at M = 6. After initial ligament formation, the liquid structures transition from individual ligaments to ensembles that appear web-like, as shown in Figure 11b. The webs contain ligaments, identified as “C” and ligaments with bulges and necking, identified as “D”. Many of the ligaments are connected by liquid sheets, identified as “E”. These web-like structures are highly dynamic, and as they travel downstream they start to breakup. Breakup begins with the thin liquid sheet regions, which create the smallest droplets, and then progress to ligament breakup. This process continues until the spray is composed entirely of droplets. Some

418 of the droplets contain bubbles (Figure 11c), and some form mushroom-like structures (Figure
419 11d). In both cases, these structures are smaller than those observed with M = 6.

420 Figure 12 provides a series of images separated by 278 μs showing the expansion and
421 breakup of a web-like structure. Note the primary shapes in each image change from frame-to-
422 frame due to the shear forces imparted on the liquid from the gas stream. Many of the larger
423 structures in Figure 12 elongate and undergo secondary breakup. When secondary breakup
424 occurs at M = 30, the process starts in a similar fashion to that observed with M = 6, where
425 droplets first deform into a thin oblong shape. The center region of the oblong shape then
426 narrows as the edges pull apart. It is common to see the oblong shape get stretched into a thin
427 ligament and break into multiple droplets if enough liquid mass is present. It is also common to
428 see a small bag form near the center of the oblong shape, which abruptly disappears upon
429 secondary breakup. A series of images, separated by 278 μs, showing an oblong object forming a
430 bag and then breaking up is shown in Fig. 13. Note, this bag formation process is similar to that
431 observed with M = 6, but the bags and resulting droplets are much smaller at the higher gas flow
432 rate with M = 30.

433 The majority of the liquid spray mass continues to sweep across the spray field even
434 when the spray is all droplets. Backlit visible light imaging at this condition shows that this
435 sweeping motion is due to the upstream oscillatory motion, where the liquid continues to move
436 in the direction that is observed upstream.

437 3.3.3 Airblast atomizer with M > 30

438 The spray dynamics are similar when $30 \leq M \leq 66$, but change considerably when
439 M = 95 ($66 < M < 95$ were not visualized). Most of the formation phenomena occur very near
440 the nozzle exit. Figure 14 shows sample images at the nozzle exit for various gas flow rates

441 while SR = 0. All of these images were acquired with the SA-Z camera and the specific camera
442 frame rates and image sizes are summarized in Table 1. Note the physical scale of each image is
443 identical. The image (x, y) coordinate that identifies the image center relative to the liquid needle
444 exit is also provided. Additionally, videos for each of these conditions can be found in the
445 supplemental material (for paper production team: Please add link to supplemental material,
446 which have been uploaded to the journal submission web site).

447 Recall that the liquid needle has an ID of d_l = 2.1 mm ID and an OD of D_l = 2.7 mm; this
448 is represented in Figure 14 with the black bars on top of each image. When M = 6, the liquid
449 intact length extends beyond the image region. Bags also continuously form and extend beyond
450 the image region. The liquid has been observed to wick up the outer diameter of the liquid needle
451 so as it exits nozzle, the intact liquid core extends spanwise beyond the inner wall. This has also
452 been shown numerically if the wetting dynamics are properly modeled (Vu et al., 2021).

453 Increasing the momentum flux ratio to M = 30 causes the liquid region to narrow as it
454 exits the liquid needle and appear to oscillate in this 2D projection. Bags that do form for this
455 flow condition are short-lived and breakup into ligaments that appear to be pulled from the liquid
456 region. Air bubbles are also observed to form in the liquid region of the image, and some are
457 transported into the next image region while others disappear as they pop.

458 Similar dynamics are observed when M = 48 and M = 66. The main difference is the
459 intact length decreases with increasing M. When M = 95, the flow structure appears to form an
460 upside-down crown, where the inside of the crown is a depressed region of low liquid content. It
461 is hypothesized that as high velocity gas exits the nozzle around the periphery of the slower
462 liquid region, a toroidal recirculation cell forms with high velocity gas pushing the liquid
463 upstream in the center of the liquid needle. This results in liquid being pulled from the outer

region and a liquid depression forms in the inner region, creating the crown. Machicoane et al. (Machicoane et al., 2019) have shown that when swirl is added to this flow, the crown formation occurs at lower momentum flux ratios.

Increasing the momentum flux ratio to M = 150 reveals the crown walls periodically get very short such that a portion may disappear. Using the aluminum outer air nozzle, Machicoane et al. (Machicoane et al., 2019) showed that when this happens, the crown partially dewets from a portion of the liquid needle exit, and this process is very dynamic; they called this flow "unstable crown". Air bubbles also periodically form in the inner region of the crown and then dissipate.

Further increasing the gas flow rate to M = 210 shortens the crown region and it still remains unstable. Some of the liquid ligaments that are pulled from the crown edges are caught in the recirculation cells and wrap upstream as they dissipate. Air bubbles also appear to migrate upstream in the liquid flow. At the highest momentum flux ratio of M = 440, the crown is very short and still unstable. One interesting observation at this momentum flux ratio is that some of the small liquid droplets that do form migrate upstream of the flow direction in the nozzle center. We believe this happens in the center region of the liquid needle and not outside the liquid needle because the high velocity gas stream outside the liquid region would prevent liquid backflow. This confirms the presence of a toroidal recirculation cell where high velocity gas is pushing the liquid in the center of the flow in the opposite direction.

The upstream migration of air bubbles and liquid droplets is further confirmed in Figure 15, where images taken at 100 kHz are shown right at the nozzle exit for M = 210 and M = 440 with SR = 0. Note that for this image acquisition speed, the image size, which is shown on the figure, is reduced to a region smaller than the liquid needle ID and each image is centered

on the liquid needle centerline. Each image in the shown sequence is separated by 50 μs (every 5th image at a frame rate of 100 kHz). When M = 210, the air bubble caught in the interior of the liquid crown migrates upstream over the 200 μs time frame, as shown by the white circled region. When M = 440, a liquid droplet is identified in the white circled region and it also migrates upstream over the given time period. It is unlikely that observations such as those shown in Figures 14 and 15 could be made with backlit or shadowgraph imaging.

4 Future Applications and Challenges

High-speed white beam imaging is a powerful flow visualization technique that can be used to capture high-speed multiphase flows that are obscured when using visible light or lasers. The current work shows qualitative observations. Quantitative measures of equivalent path length (EPL), defined as the accumulated liquid along the beam path, are easily acquired using focused beam measurements (Bothell et al., 2020a; Kastengren et al., 2014; Li et al., 2019). In this imaging mode, Beer-Lambert's Law can be used to determine EPL:

$$\mathrm{EPL} = \ell = \frac{1}{\mu} \ln\left[\frac{I_0}{I(t)}\right] \tag{7}$$

where μ is the attenuation coefficient. In white beam imaging, however, μ is not known precisely because it is a function of X-ray wavelength, and white beam imaging has a variety of wavelengths, which are differentially attenuated, depending on the material and material thickness. This complicates the analysis, but with proper calibration and X-ray energy modeling, the white beam-determined EPL may be approximated; this is the focus of some of our future efforts.

Additionally, quantitative image analysis to determine droplet size and velocity will be completed in the future. Challenges remain, however, in that multiple droplets imaged with

X-rays can be easily tracked with the human eye, even when they overlap for a period of time. Developing imaging analysis tracking software that reliably captures these droplets is more complicated due to overlapping structures and small variations in X-ray image contrast.

Another challenge is that the X-ray beam from the APS synchrotron facility is limited in size, so the maximum field of view is only ~8 mm wide by ~6 mm tall. Additionally, the beam flux near the edges of the beam are not as uniform or steady as near the center, and these fluctuations will create X-ray image contrast variations with time and location.

Finally, the X-ray beams generated at APS are fixed in space and correspond to tangents of the synchrotron ring. Hence, X-ray flow visualization from multiple projections at the same instant in time, like those from two or more tube X-ray sources (Halls et al., 2019; Heindel et al., 2008; Mudde, 2010), is extremely challenging. One group has attempted this (Hoshino et al., 2011), but their synchrotron beam width was very large (~300 mm), and only two projections were acquired simultaneously with an angle between the projections of only about 15°.

One possible method to do computed tomography of sprays using white beam imaging is to mount the spray on a rotation system, and then rotate the spray to produce the multiple views required for tomographic reconstruction. If the spray is periodic like a liquid fuel injector, it is possible to phase-lock the measurements to produce time-resolved 3D images, assuming the injection process is highly repeatable (Tekawade et al., 2020). Additionally, to view multiple spray locations for larger sprays like the one used in this study, the spray has to be mounted on an x-y translation stage. The desire to look at pressurized spray systems requires a small pressurized spray facility where the entire system can be mounted on an x-y translation stage (Kastengren et al., 2009), or the entire spray nozzle and x-y translation stage has to be mounted within a pressured facility (Burtnett et al., 2021).

5 Conclusions

This observational study showed that high-speed white beam X-ray imaging, using the Advanced Photon Source at Argonne National Laboratory, provided unique advantages over traditional optical high-speed imaging techniques like backlit imaging. The increased detail and high temporal and spatial resolution enabled a very detailed qualitative analysis of the spray structure, dynamics, and breakup. Using a canonical airblast atomizer, overlapping bags ligaments, and bubbles were clearly observed with X-ray imaging. As the momentum flux ratio increased with a constant liquid flow rate, the atomization process moved toward the nozzle exit. Bag and ligament formation still occurred, but at a faster rate. When $M \geq 95$, an unstable crown formed at the liquid needle exit, and as the momentum flux ratio increased, the crown became shorter and more dynamic.

One unique advantage of high-speed white beam X-ray imaging is that overlapping flow structures can be captured including ligaments, droplets, mushrooms, and webs. Furthermore, air bubbles within liquid regions were clearly captured. This also allowed for the observation that air bubbles and liquid droplets migrated upstream within the liquid crown at the highest momentum flux ratios on this study. These structures are not observed with optical imaging techniques.

One challenge with high-speed white beam X-ray imaging is the limited field of view. To capture the entire spray region, particularly at the lower momentum flux ratios, several overlapping imaging regions were required, and some of the flow structures could not be tracked from region to region.

6 Acknowledgements

This work was sponsored by the Office of Naval Research (ONR) as part of the Multidisciplinary University Research Initiatives (MURI) Program, under grant number N00014-

16-1-2617. The Photron SA-Z camera was purchased as part of the ONR DURIP program, under grant number N00014-18-1-2380. The views and conclusions contained herein are those of the authors only and should not be interpreted as representing those of ONR, the U.S. Navy, or the U.S. Government.

This work was performed at the 7-BM beamline of the Advanced Photon Source, a U.S. Department of Energy (DOE) Office of Science User Facility operated for the DOE Office of Science by Argonne National Laboratory under Contract No. DE-AC02-06CH11357. The use of their facilities and personnel is greatly appreciated.

7 References

Aliseda, A. and Heindel, T.J., X-ray Flow Visualization in Multiphase Flows, *Annual Review of Fluid Mechanics*, vol. **53**, pp. 543-567, 2021.

Anderson, I.E., White, E.M.H. and Dehoff, R., Feedstock Powder Processing Research Needs for Additive Manufacturing Development, *Current Opinion in Solid State and Materials Science*, vol. **22**, no. 1, pp. 8-15, 2018.

Bachalo, W., Spray Diagnostics for the Twenty-First Century, *Atomization and Sprays*, vol. **10**, no. 3-5, pp. 439-474, 2000.

Bothell, J.K., Machicoane, N., Li, D., Morgan, T.B., Aliseda, A., Kastengren, A.L. and Heindel, T.J., Comparison of X-ray and Optical Measurements in the Near-Field of an Optically Dense Coaxial Air-Assisted Atomizer, *International Journal of Multiphase Flow*, vol. **125**, pp. 103219, 2020a.

Bothell, J.K., Morgan, T.B. and Heindel, T.J. Image-Based Feedback Control for a Coaxial Spray, *Journal of Fluids Engineering*, vol. **142**, no. 11, pp. Paper 114501, 2020b.

577 Burtnett, T.B., Morgan, T.B., Dahlstrom, T.C., Aliseda, A. and Heindel, T.J., A Pressurized
578 Tank for High Flow Rate Atomization Studies, *ICLASS 2021, 15th Triennial International*
579 *Conference on Liquid Atomization and Spray Systems*, Edinburgh, UK, August 29 -
580 September 2, 2021.
581 Cartz, L., *Nondestructive Testing*, Materials Park, OH: ASM International, 1995.
582 Castrejón-García, R., Castrejón-Pita, J., Martin, G. and Hutchings, I., The Shadowgraph Imaging
583 Technique and Its Modern Application to Fluid Jets and Drops, *Revista mexicana de física*,
584 vol. **57**, no. 3, pp. 266-275, 2011.
585 Castrejón-Pita, J.R., Castrejón-García, R. and Hutchings, I.M., High Speed Shadowgraphy for
586 the Study of Liquid Drops, in *Fluid Dynamics in Physics, Engineering and Environmental*
587 *Applications*, J. Klapp, A. Medina, A. Cros and C.A. Vargas, Eds., Berlin: Springer, pp. 121-
588 137, 2013.
589 Coletti, F., Benson, M.J., Sagues, A.L., Miller, B.H., Fahrig, R. and Eaton, J.K., Three-
590 Dimensional Mass Fraction Distribution of a Spray Measured by X-ray Computed
591 Tomography, *Journal of Engineering for Gas Turbines and Power*, vol. **136**, no. 5, pp.
592 051508: 1-8, 2014.
593 Dash, A., Jahangir, S. and Poelma, C., Direct Comparison of Shadowgraphy and X-ray Imaging
594 for Void Fraction Determination, *Measurement Science and Technology*, vol. **29**, no. 12, pp.
595 125303, 2018.
596 Fansler, T.D. and Parrish, S.E., Spray Measurement Technology: A Review, *Measurement*
597 *Science and Technology*, vol. **26**, no. 1, pp. 1-34, 2015.

598 Halls, B.R., Heindel, T.J., Kastengren, A.L. and Meyer, T.R., Evaluation of X-ray Sources for
599 Quantitative Two- and Three-Dimensional Imaging of Liquid Mass Distribution in
600 Atomizing Sprays, *International Journal of Multiphase Flow*, vol. **59**, pp. 113-120, 2014.
601 Halls, B.R., Radke, C.D., Reuter, B.J., Kastengren, A.L., Gord, J.R. and Meyer, T.R., High-
602 Speed, Two-Dimensional Synchrotron White-Beam X-ray Radiography of Spray Breakup
603 and Atomization, *Optics Express*, vol. **25**, no. 2, pp. 1605-1617, 2017.
604 Halls, B.R., Rahman, N., Slipchenko, M.N., James, J.W., McMaster, A., Ligthfoot, M.D.A.,
605 Gord, J.R. and Meyer, T.R., 4D Spatiotemporal Evolution of Liquid Spray Using Kilohertz-
606 Rate X-ray Computed Tomography, *Optics Letters*, vol. **44**, no. 20, pp. 5013-5016, 2019.
607 Hampel, U., Image Reconstruction for Hard Field Tomography, in *Industrial Tomography:*
608 *Systems and Applications*, M. Wang, Ed. Waltham, MA: Elsevier: pp. 347-376, 2015.
609 Heindel, T.J., A Review of X-ray Flow Visualization with Applications to Multiphase Flows,
610 *ASME Journal of Fluids Engineering*, vol. **133**, no. 7, pp. 074001, 2011.
611 Heindel, T.J., X-ray Imaging Techniques to Quantify Spray Characteristics in the Near-Field,
612 *Atomization and Sprays*, vol. **28**, no. 11, pp. 1029-1059, 2018.
613 Heindel, T.J., Gray, J.N. and Jensen, T.C., An X-ray System for Visualizing Fluid Flows, *Flow*
614 *Measurement and Instrumentation*, vol. **19**, no. 2, pp. 67-78, 2008.
615 Heindel, T.J., Morgan, T.B., Burtnett, T.J., Bothell, J.K., Li, D., Aliseda, A. and Machicoane, N.,
616 High-Speed Flow Visualization of a Canonical Airblast Atomizer Using Synchrotron X-rays,
617 *AJK2019 - Joint ASME/JSME/KSME Fluids Engineering Division Summer Meeting*, San
618 Francisco, CA, July 28 - August 1, ASME Press, Paper Number: AJKFLUIDS2019-4992,
619 2019.

620 Hoshino, M., Uesugi, K., Pearson, J., Sonobe, T., Shirai, M. and Yagi, N., Development of an
621 X-ray Real-Time Stereo Imaging Technique Using Synchrotron Radiation, *Journal of*
622 *Synchrotron Radiation*, vol. **18**, no. 4, pp. 569-574, 2011.
623 Hsieh, J., *Computed Tomography: Principles, Design, Artifacts, and Recent Advances*,
624 Bellingham, WA: SPIE Press, 2003.
625 Huck, P.D., Machicoane, N., Osuna-Orozcon, R. and Aliseda, A., Experimental Characterization
626 of a Canonical Two-Fluid Coaxial Atomizer, *ICLASS 2018, 14th Triennial International*
627 *Conference on Liquid Atomization and Spray Systems*, Chicago, IL, July 22-26, 2018.
628 Karathanassis, I.K., Heidari-Koochi, M., Zhang, Q., Hwang, J., Koukouvinis, P., Wang, J. and
629 Gavaises, M., X-ray Phase Contrast and Absorption Imaging for the Quantification of
630 Transient Cavitation in High-Speed Nozzle Flows, *Physics of Fluids*, vol. **33**, no. 3, pp.
631 032102, 2021.
632 Kastengren, A.L. and Powell, C., Synchrotron X-ray Techniques for Fluid Dynamics,
633 *Experiments in Fluids*, vol. **55**, no. 3, pp. 1-15, 2014.
634 Kastengren, A.L., Powell, C.F., Arms, D., Dufresne, E.M., Gibson, H. and Wang, J., The 7BM
635 Beamline at the APS: A Facility for Time-Resolved Fluid Dynamics Measurements, *Journal*
636 *of Synchrotron Radiation*, vol. **19**, no. 4, pp. 654-657, 2012.
637 Kastengren, A.L., Powell, C.F., Wang, Y., Im, K.-S. and Wang, J., X-ray Radiography
638 Measurements of Diesel Spray Structure at Engine-Like Ambient Density, *Atomization and*
639 *Sprays*, vol. **19**, no. 11, pp. 1031-1044, 2009.
640 Kastengren, A.L., Tilocco, F.Z., Duke, D.J., Powell, C.F., Zhang, X. and Moon, S., Time-
641 Resolved X-ray Radiography of Sprays from Engine Combustion Network Spray a Diesel
642 Injectors, *Atomization and Sprays*, vol. **24**, no. 3, pp. 251-272, 2014.

643 Khlifa, I., Vabre, A., Hočevar, M., Fezzaa, K., Fuzier, S., Roussette, O. and Coutier-Delgosha,
644 O., Fast X-ray Imaging of Cavitating Flows, *Experiments in Fluids*, vol. **58**, no. 11, pp. 157,
645 2017.
646 Li, D., Bothell, J.K., Morgan, T.B., Heindel, T.J., Aliseda, A., Machicoane, N. and Kastengren,
647 A.L., High-Speed X-ray Imaging of an Airblast Atomizer at the Nozzle Exit, *2017 APS-DFD*
648 *Meeting*, Denver, CO, November 19 - 21, 2017, APS-DFD Gallery of Fluid Motion Video
649 Entry #V0026, https://doi.org/10.1103/APS.DFD.2017.GFM.V0026, 2017a.
650 Li, D., Morgan, T.B., Pulfer, L.D. and Heindel, T.J., Measurement of near-Field Spray
651 Characteristics with Broadband X-rays, *ASME 2017 FEDSM - Fluids Division Summer*
652 *Meeting*, Hilton Waikoloa Village, Waikoloa, Hawaii, July 30 - August 3, ASME Press,
653 Paper Number FEDSM2017-69088, 2017b.
654 Li, D., Bothell, J.K., Morgan, T.B., Machicoane, N., Aliseda, A., Kastengren, A.L. and Heindel,
655 T.J., Time-Averaged Spray Analysis in the Near-Field Region Using Broadband and
656 Narrowband X-ray Measurements, *Atomization and Sprays*, vol. **29**, no. 4, pp. 331-349,
657 2019.
658 Lightfoot, M.D., Schumaker, S.A., Danczyk, S.A. and Kastengren, A.L., Core Length and Spray
659 Width Measurements in Shear Coaxial Rocket Injectors from X-Ray Radiography
660 Measurements, *ILASS Americas: 27th Annual Conference on Liquid Atomization and Spray*
661 *Systems*, Raleigh, NC, May 2015.
662 Lin, K.-C., Kastengren, A.L. and Carter, C., Exploration of Temporal and Time-Averaged Two-
663 Phase Flow Structures Using X-ray Diagnostics, *ILASS Americas: 29th Annual Conference*
664 *on Liquid Atomization and Spray Systems*, Atlanta, GA, May 15-18, 2017.

665 Linne, M., Analysis of X-ray Phase Contrast Imaging in Atomizing Sprays, *Experiments in*
666 *Fluids*, vol. **52**, no. 5, pp. 1201-1218, 2012a.
667 Linne, M., Analysis of X-ray Radiography in Atomizing Sprays, *Experiments in Fluids*, vol. **53**,
668 no. 3, pp. 655-671, 2012b.
669 Linne, M., Imaging in the Optically Dense Regions of a Spray: A Review of Developing
670 Techniques, *Progress in Energy and Combustion Science*, vol. **39**, no. 5, pp. 403-440, 2013.
671 Machicoane, N. and Aliseda, A., Experimental Characterization of a Canonical Coaxial Gas-
672 Liquid Atomizer, *ILASS - Americas 2017: 29th Annual Conference on Liquid Atomization*
673 *and Spray Systems*, Atlanta, GA, May 15-18, 2017.
674 Machicoane, N., Bothell, J.K., Li, D., Morgan, T.B., Heindel, T.J., Kastengren, A.L. and
675 Aliseda, A., Synchrotron Radiography Characterization of the Liquid Core Dynamics in a
676 Canonical Two-Fluid Coaxial Atomizer, *International Journal of Multiphase Flow*, vol. **115**,
677 pp. 1-8, 2019.
678 Matusik, K.E., Sforzo, B.A., Seong, H.J., Duke, D., Kastengren, A., Ilavsky, J. and Powell, C.F.,
679 X-ray Measurements of Fuel Spray Specific Surface Area and Sauter Mean Diameter for
680 Cavitating and Non-Cavitating Diesel Sprays, *Atomization and Sprays*, vol. **29**, no. 3, pp.
681 199-216, 2019.
682 Moon, S., Gao, Y., Park, S., Wang, J., Kurimoto, N. and Nishijima, Y., Effect of the Number and
683 Position of Nozzle Holes on in- and Near-Nozzle Dynamic Characteristics of Diesel
684 Injection, *Fuel*, vol. **150**, pp. 112-122, 2015.
685 Morgan, T.B. and Heindel, T.J., An Automated System for Systematic Spray Expansion Angle
686 Measurements," *ILASS-AMERICAS 2021, 31st Annual Conference on Liquid Atomization*
687 *and Spray Systems*, Virtual, May 16-19, 2021.

688 Mudde, R.F., Double X-ray Tomography of a Bubbling Fluidized Bed, *Industrial & Engineering*
689 *Chemistry Research*, vol. **49**, no. 11, pp. 5061-5065, 2010.
690 Osta, A.R., Lee, J., Sallam, K.A. and Fezzaa, K., Study of the Effects of the Injector
691 Length/Diameter Ratio on the Surface Properties of Turbulent Liquid Jets in Still Air Using
692 X-ray Imaging, *International Journal of Multiphase Flow*, vol. **38**, no. 1, pp. 87-98, 2012.
693 Rahman, N., Halls, B.R., James, J.W., McMaster, A., Lightfoot, M.D.A., Gord, J.R. and Meyer,
694 T.R., 4D Imaging of Primary Liquid Breakup Using High-Speed Tomographic X-ray
695 Radiography, *ICLASS 2018, 14th Triennial International Conference on Liquid Atomization*
696 *and Spray Systems*, Chicago, IL, July 22-26, 2018.
697 Settles, G.S. and Hargather, M.J., A Review of Recent Developments in Schlieren and
698 Shadowgraph Techniques, *Measurement Science and Technology*, vol. **28**, no. 4, pp. 042001,
699 2017.
700 Tekawade, A., Sforzo, B.A., Matusik, K.E., Fezzaa, K., Kastengren, A.L. and Powell, C.F.,
701 Time-Resolved 3D Imaging of Two-Phase Fluid Flow Inside a Steel Fuel Injector Using
702 Synchrotron X-ray Tomography, *Scientific Reports*, vol. **10**, no. 1, pp. 8674, 2020.
703 Van Nieuwenhove, V., De Beenhouwer, J., De Carlo, F., Mancini, L., Marone, F. and Sijbers, J.,
704 Dynamic Intensity Normalization Using Eigen Flat Fields in X-ray Imaging, *Optics Express*,
705 vol. **23**, no. 21, pp. 27975-27989, 2015.
706 Vu, L., Machicoane, N., Li, D., Morgan, T.B., Heindel, T.J., Aliseda, A. and Desjardins, O.,
707 Validation of Inflow Modeling Strategies for Numerical Simulations of Air-Blast
708 Atomization against Experimental Backlit Imaging and Radiographs, *ILASS-AMERICAS*
709 *2021, 31st Annual Conference on Liquid Atomization and Spray Systems*, Virtual, May 16-
710 19, 2021.

Zhang, G., Khlifa, I. and Coutier-Delgosha, O., A Comparative Study of Quasi-Stable Sheet Cavities at Different Stages Based on Fast Synchrotron X-ray Imaging, *Physics of Fluids*, vol. **32**, no. 12, pp. 123316, 2020a.

Zhang, G., Khlifa, I., Fezzaa, K., Ge, M. and Coutier-Delgosha, O., Experimental Investigation of Internal Two-Phase Flow Structures and Dynamics of Quasi-Stable Sheet Cavitation by Fast Synchrotron X-ray Imaging, *Physics of Fluids*, vol. **32**, no. 11, pp. 113310, 2020b.

Tables

Table 1: Gas flow rates and camera settings for the nozzle exit images shown in Figure 14. The liquid flow rate was fixed for all conditions at Re_l = 1,100 (Q_l = 0.099 LPM) and SR = 0.

Q_g (SLPM)	Re_g	M	Frame rate (kHz)	Frame size, H × V (pixels)	Frame size, H × V (mm)
150	21,300	6	36	896 × 640	4.82 × 3.56
330	46,700	30	36	896 × 640	4.82 × 3.56
420	59,600	48	45	640 × 664	3.56 × 3.69
490	69,600	66	45	640 × 664	3.56 × 3.69
590	83,800	95	45	640 × 664	3.56 × 3.69
730	104,000	150	67.2	512 × 520	2.84 × 2.89
870	124,000	210	67.2	512 × 520	2.84 × 2.89
1270	180,000	440	60	768 × 424	3.05 × 1.68

723 **Figures**

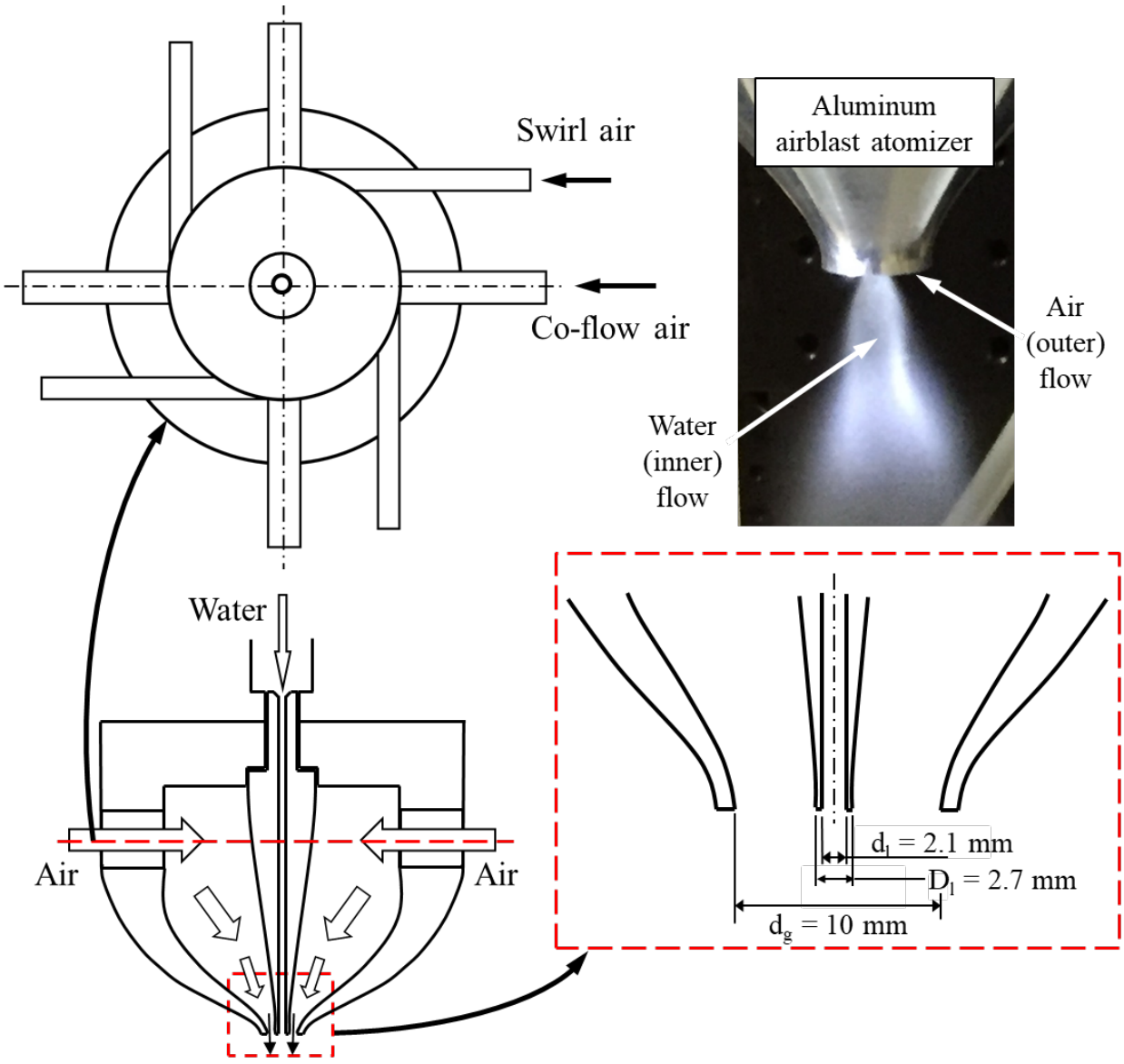

724

725 Figure 1: Airblast atomizer used in this study.

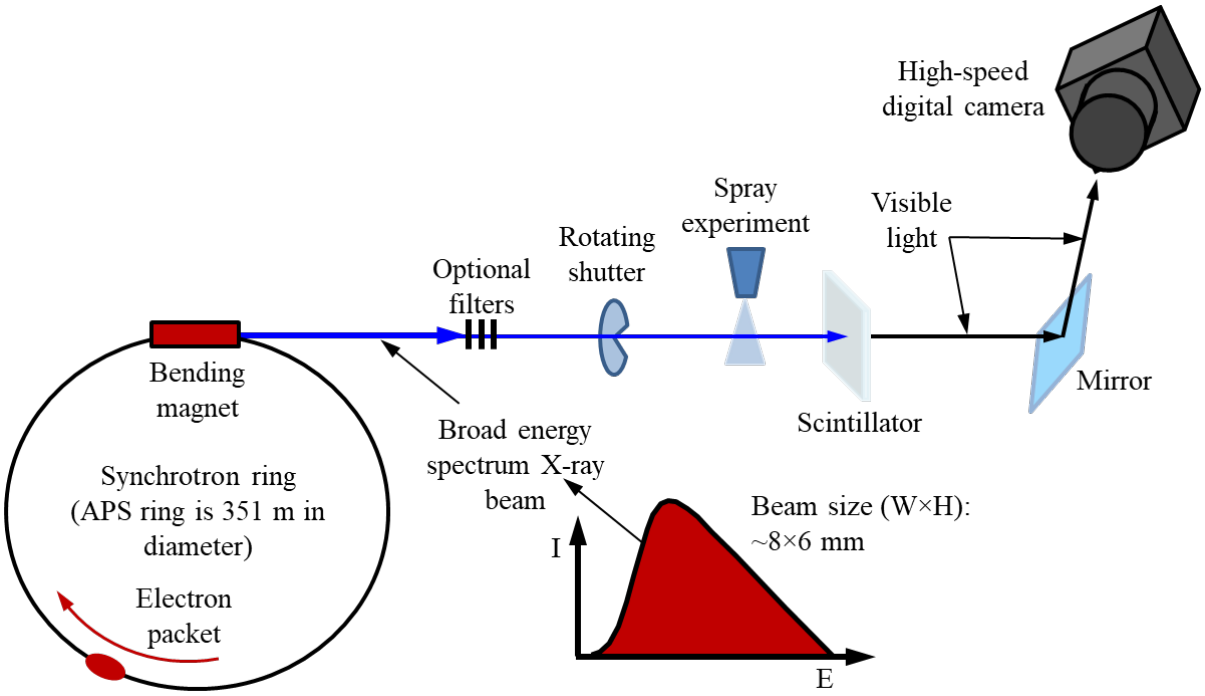

726

727 Figure 2: Schematic of the Advanced Photon Source (APS) experimental setup for high-speed

728 white beam imaging (not to scale).

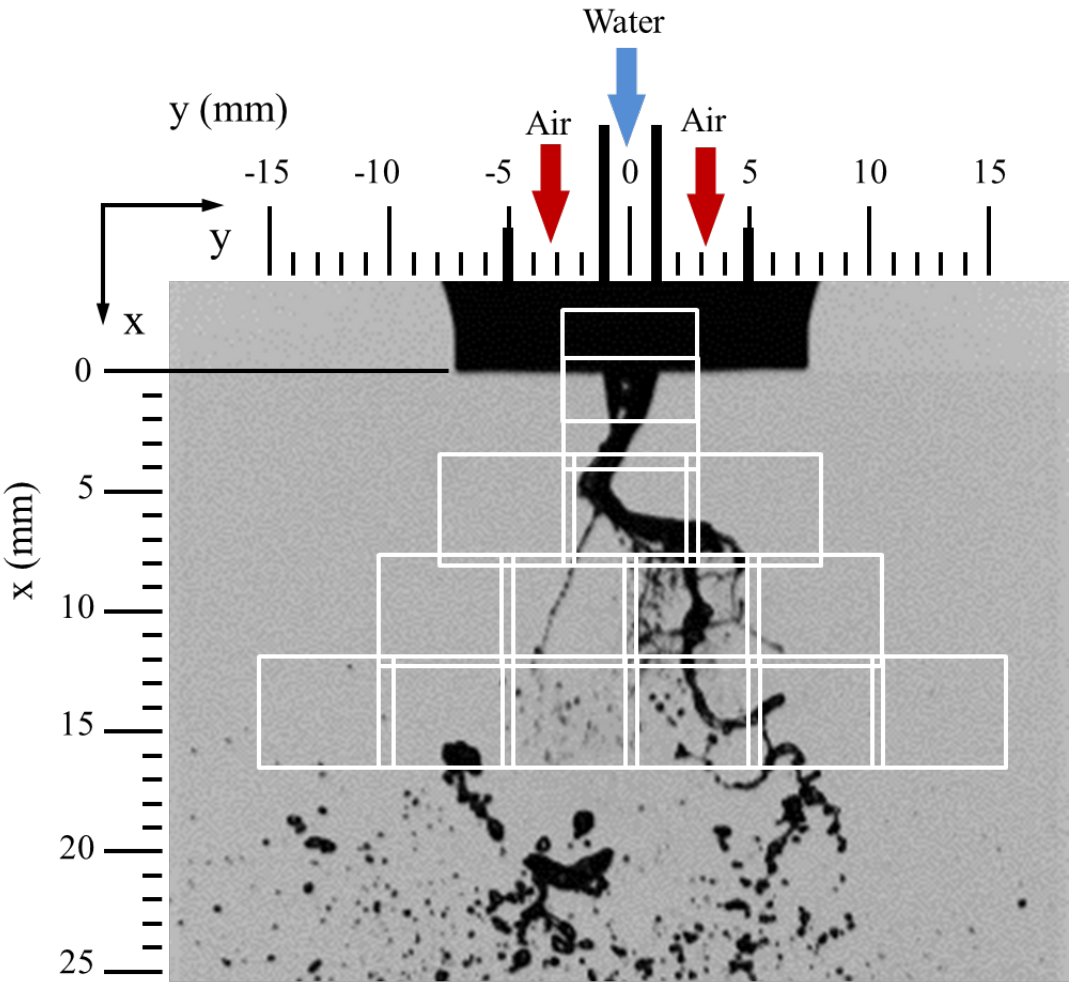

729

730 Figure 3: Sample of overlapping image regions for white beam radiography (white boxes)
731 overlaid on a backlit image of a representative spray with M = 6 and SR = 0 (units
732 in mm).

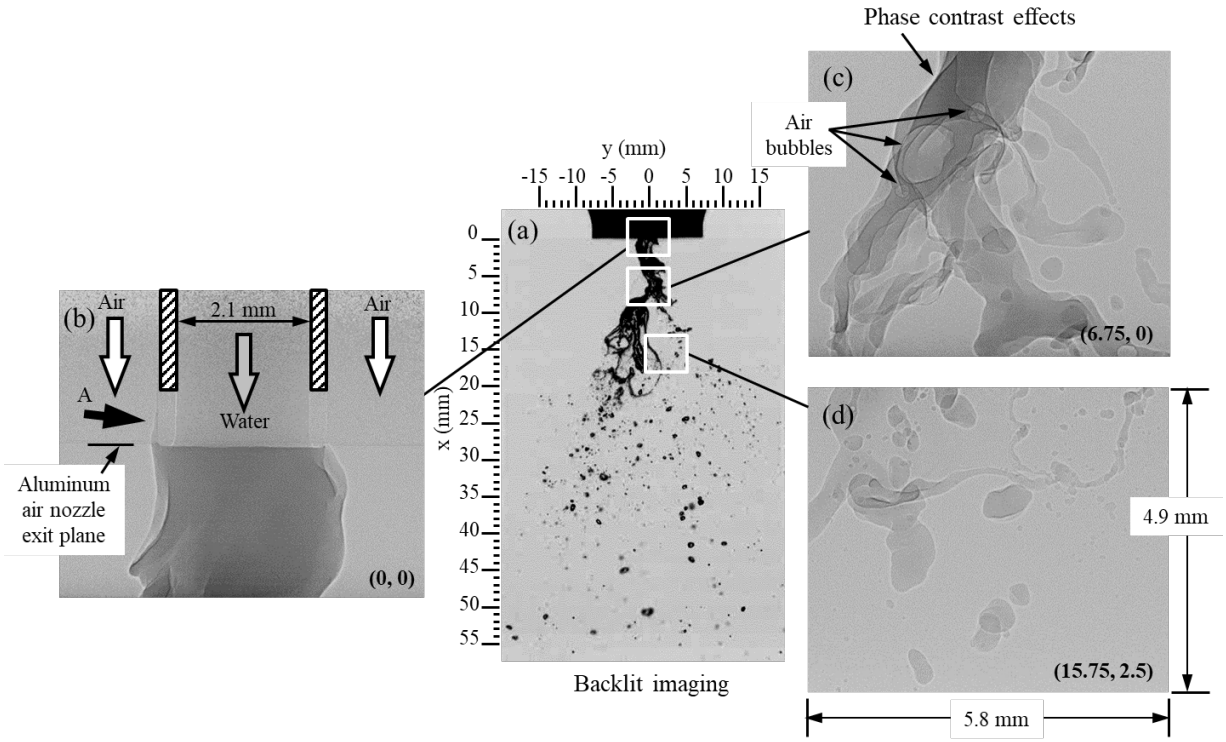

Figure 4: Co-axial spray with M = 6 and SR = 1. (a) Backlit image of large spray region. (b) White beam X-ray image at the nozzle exit, (0, 0). (c) White beam X-ray image downstream of the nozzle exit, (6.75, 0). (b) White beam X-ray image further downstream, (15.75, 2.5). All coordinate locations correspond to the (x, y) image center and are given in mm.

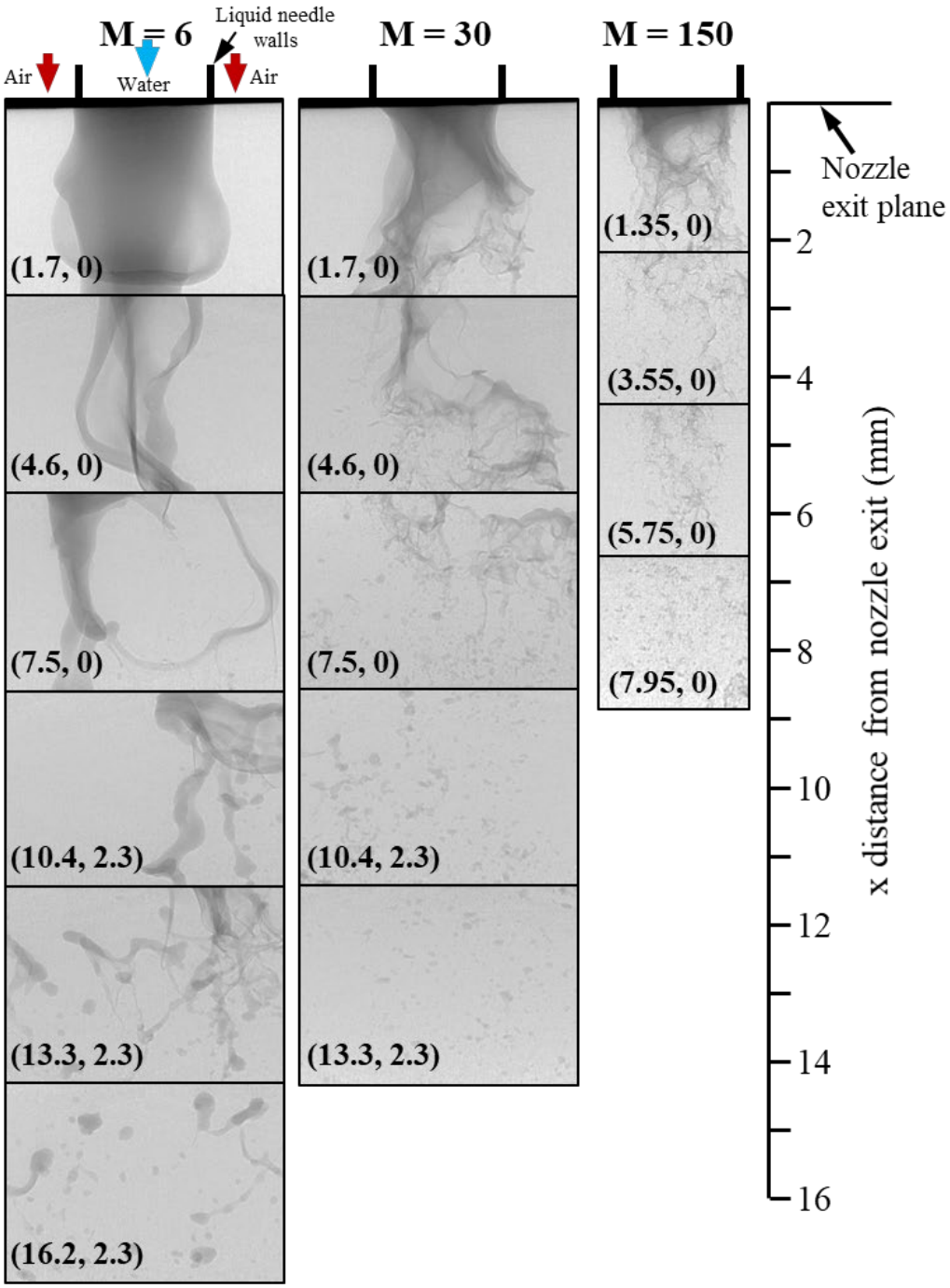

739

740 Figure 5: White beam X-ray images of an airblast atomizer showing how the spray changes in
741 response to increasing the momentum flux ratio and downstream distance. Coordinate
742 locations correspond to the (x, y) image center and are given in mm. Note lower
743 images are slightly off-center.

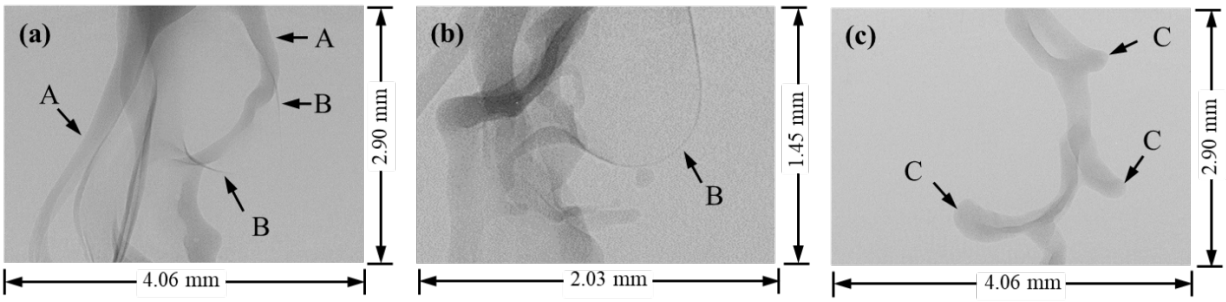

Figure 6: Selected spray structures observed with white beam X-ray imaging from an airblast atomizer with M = 6 and SR = 0. (a) Initial ligament formation; (b) bags, ligaments, and thin liquid sheets (note the image size has been increased for emphasis); and (c) secondary bag and ligament formation.

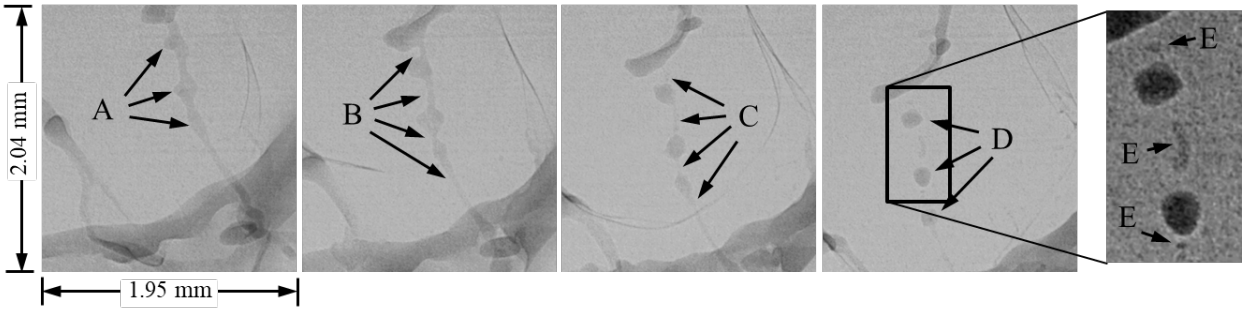

Figure 7: Ligament breakup at M = 6 with time between frames of 555 μs. Structures identified as bulges (A), thin liquid regions connecting the bulges (B and C), thin regions rupture forming droplets (D) and satellite droplets (E).

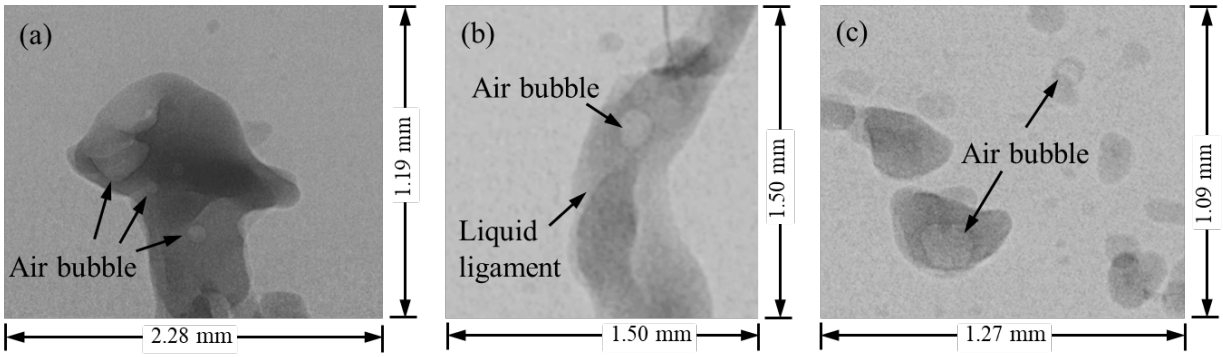

Figure 8: Sample spray structures recorded with white beam X-ray imaging with M = 6: (a) a mushroom-like structure, (b) an air bubble inside a liquid ligament, and (c) air bubbles inside liquid droplets. Note the image size varies to emphasize the given structure.

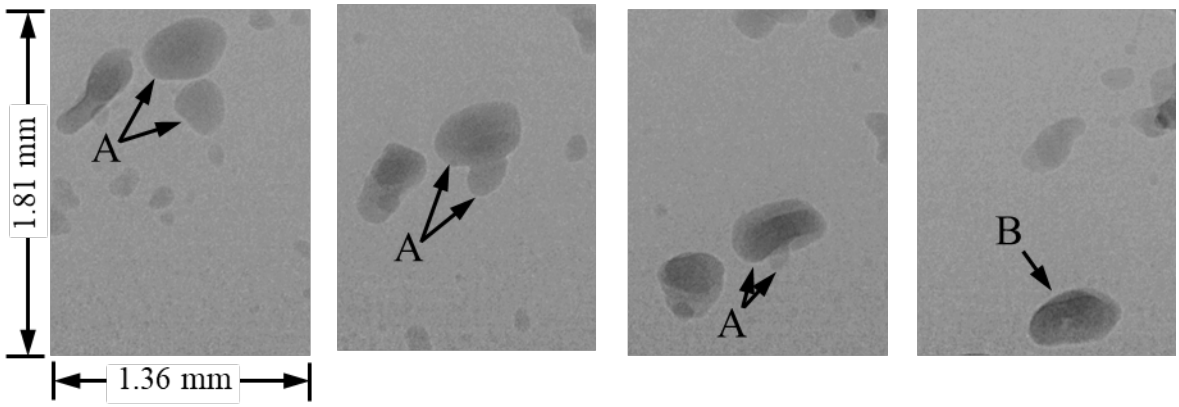

Figure 9: Droplet collision at M = 6 with time between frames of 1.1 ms. The two original droplets (A) and the coalesced droplet (B).

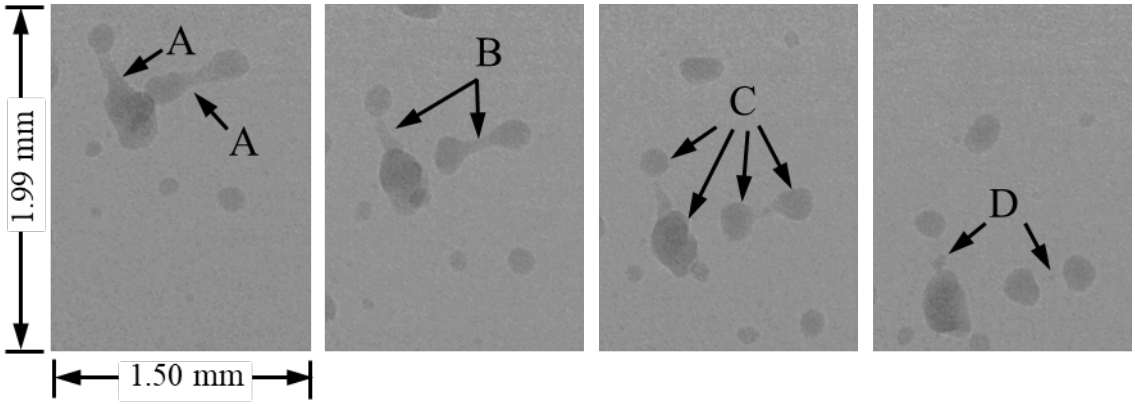

Figure 10: Secondary droplet breakup with M = 6. Oblong structures (A) are first elongated and stretched (B). The elongated droplets break and form secondary droplets (C) and satellite droplets (D).

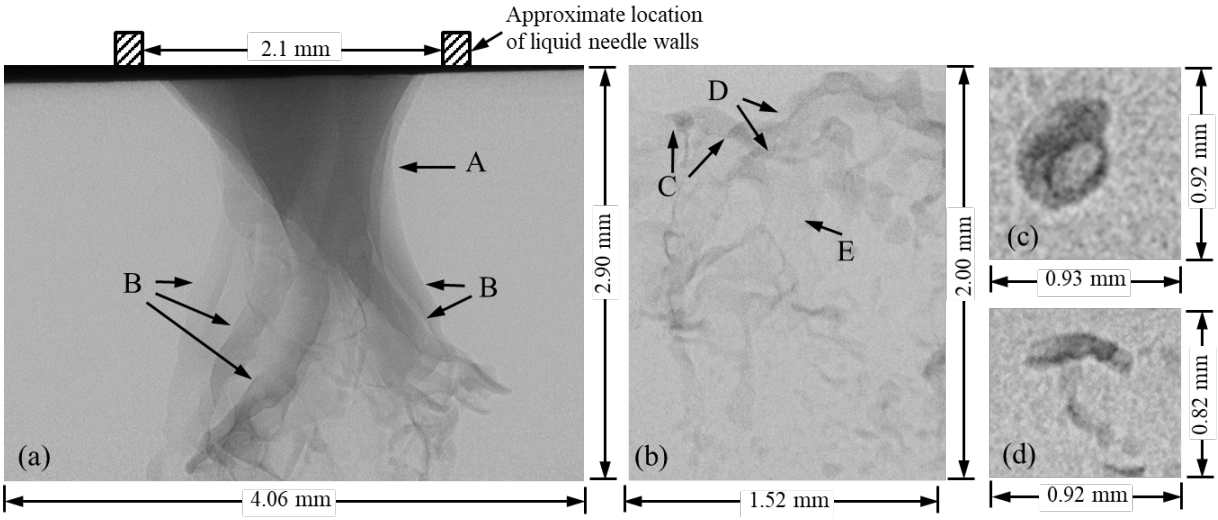

Figure 11: Spray formations seen in white beam X-ray images from a coaxial spray with M = 30 and SR = 0. (a) Liquid necking (A) and ligament formation (B); (b) liquid web structure containing liquid ligaments (C), ligament bulges and necking (D), and liquid sheets connecting the ligaments (E); (c) bubble in a liquid droplet; and (d) mushroom-like structure.

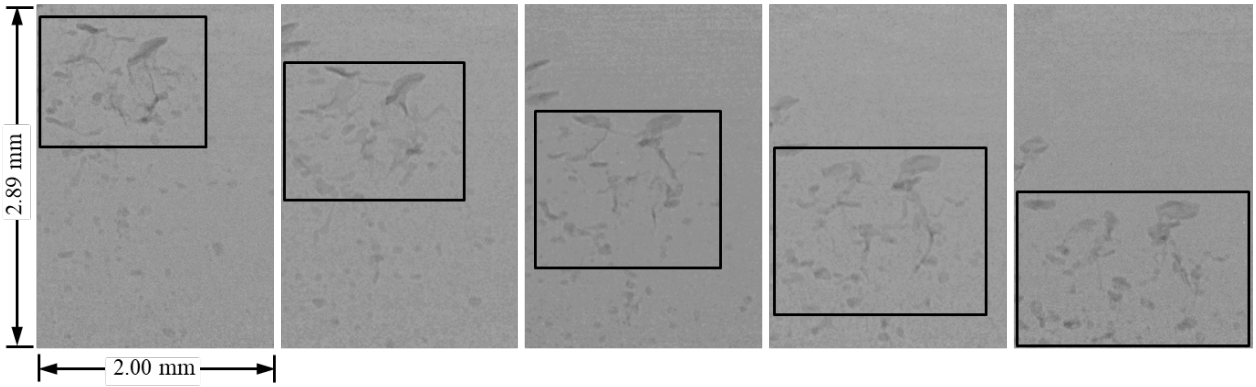

Figure 12: Downstream spray web-like structures observed with white beam X-ray imaging and M = 30. Each image is separated by 278 μs. The black box tracks a web-like structure as it moves through the spray field, expanding and breaking apart.

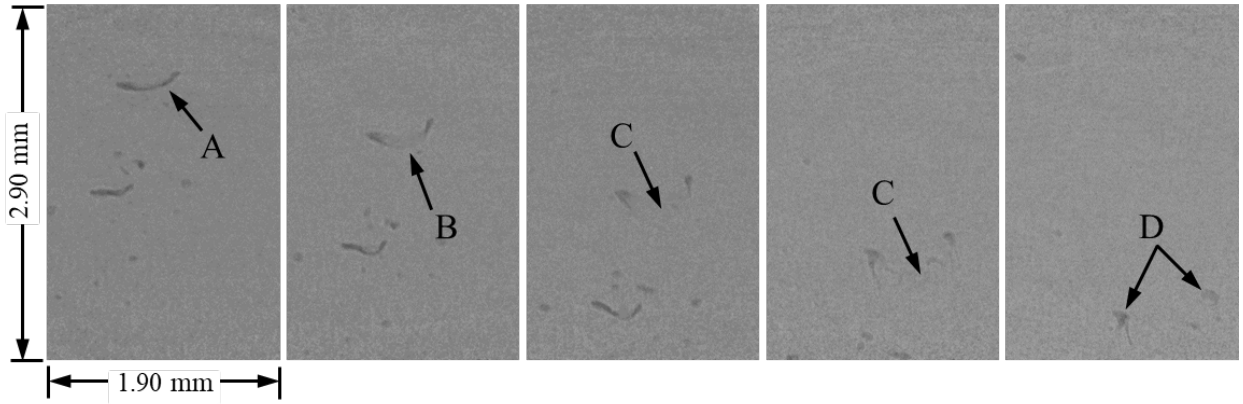

Figure 13: Secondary breakup at M = 30. Each image is separated by 278 μs. Stretching of the initial droplet into an oblong shape (A), which then undergoes bag formation (B) and breakup (C), that leads to two resulting droplets (D).

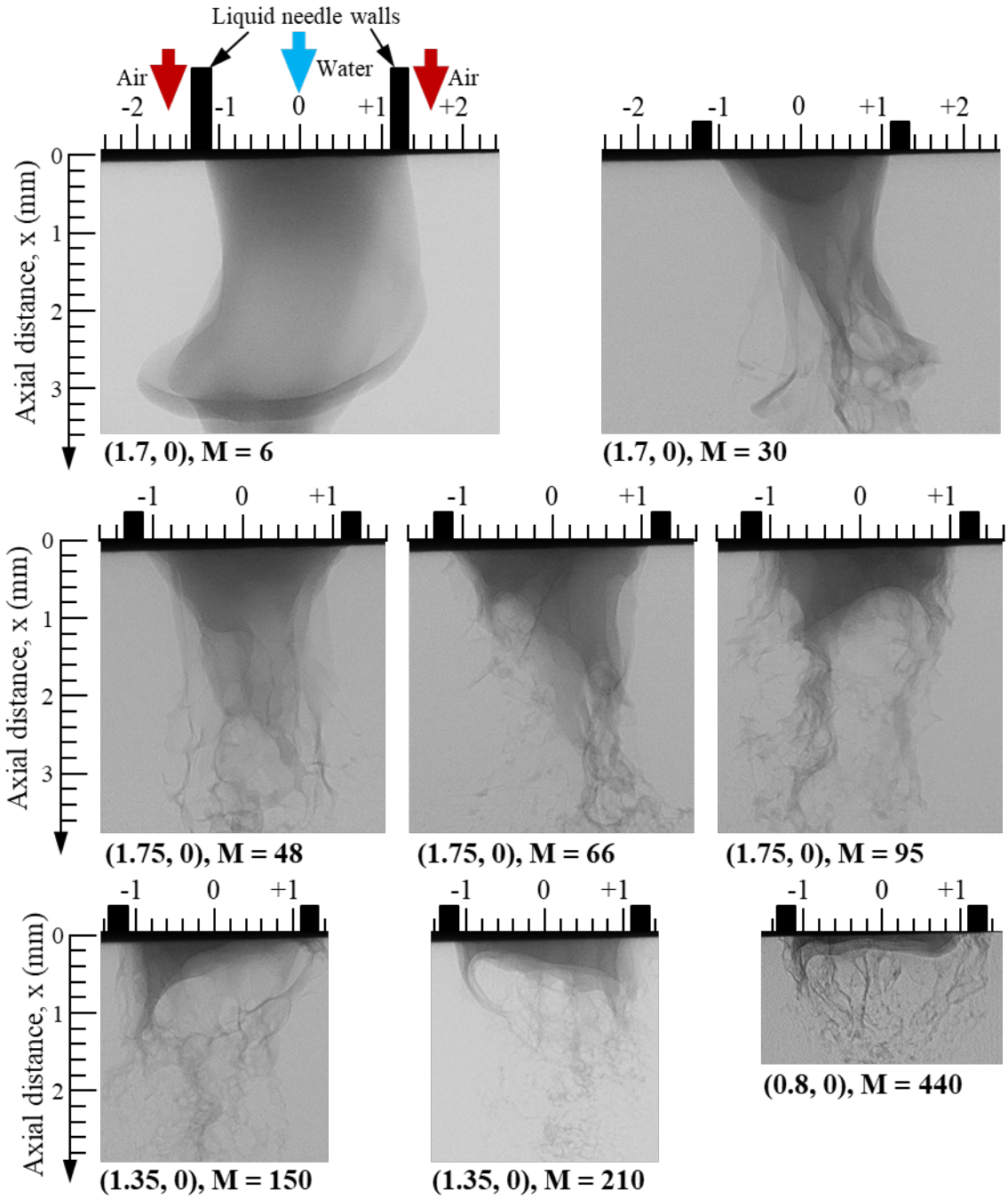

779

780 Figure 14: White beam X-ray images right at the nozzle exit for various momentum flux ratios,
781 while SR = 0 and the liquid flow rate is fixed at Re_l = 1,100. Specific flow conditions
782 are summarized in Table 1. Coordinate locations correspond to the (x, y) image center
783 and are given in mm, which also represents the scale in each image.

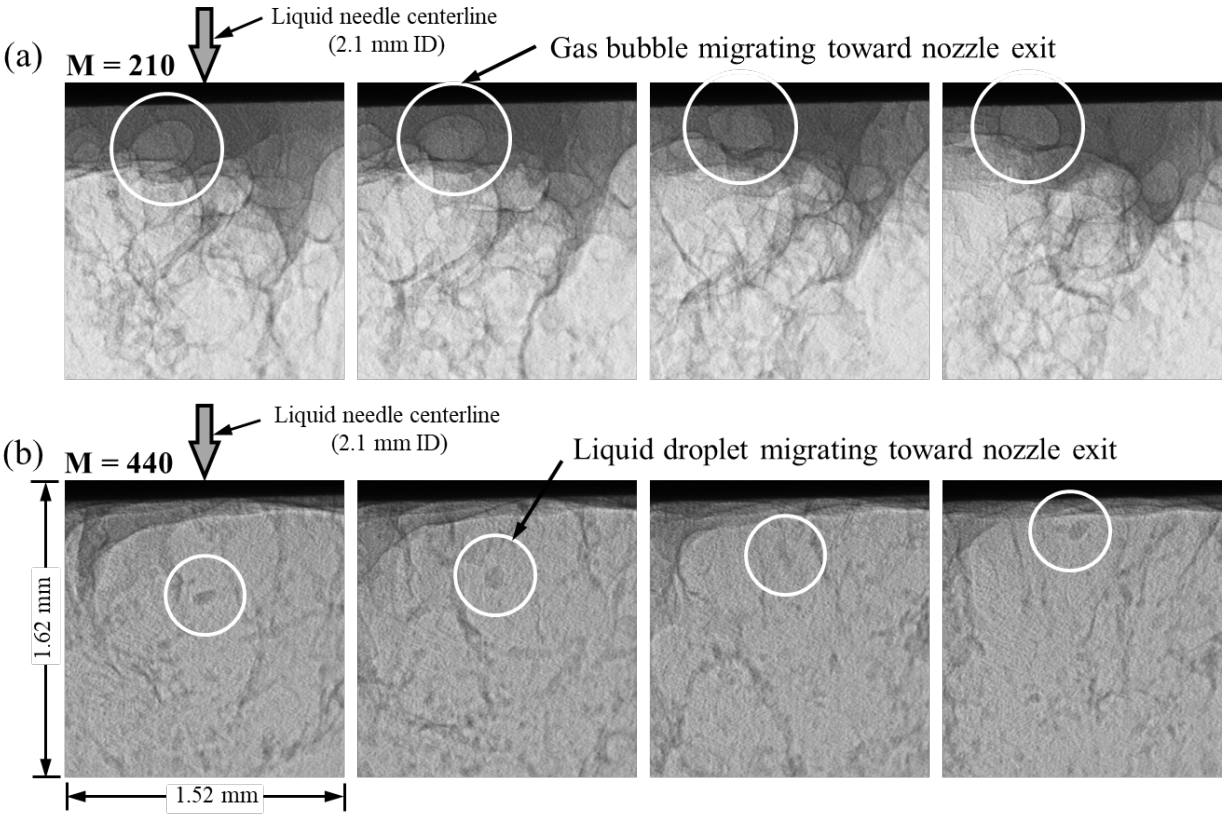

784

785 Figure 15: Close-up images taken at 100 kHz right at the exit of the liquid needle for

786 (a) M = 210 showing the upstream migration of an air bubble, and (b) M = 440

787 showing the upstream migration of a liquid droplet. The time between frames for each

788 sequence is 50 μs.